Article

Not peer-reviewed version

Innovations in Additive Manufacturing: Pressure Capacity Assessment of L-PBF Produced Microchannel Heat Exchangers for Industrial Applications

Jiabao An , Luyao Guo , Junjia Zou , Keliang Zhang , Yiheng Zhong , Taimingwang Liu , Long Huang , Yi Chen *

Posted Date: 17 July 2024

doi: 10.20944/preprints202407.1410.v1

Keywords: Laser Powder Bed Fusion (L-PBF); Microchannel Heat Exchangers; Channel Pressure Capacity; Tube Porosity; Experimental Design

Article

Innovations in Additive Manufacturing: Pressure Capacity Assessment of L-PBF Produced Microchannel Heat Exchangers for Industrial Applications

Jiabao An, Luyao Guo †, Junjia Zou †, Keliang Zhang †, Yiheng Zhong, Taimingwang Liu, Long Huang and Yi Chen *

School of Intelligent Manufacturing Ecosystem, XJTLU Entrepreneur College (Taicang), Xi'an Jiaotong-Liverpool University, Suzhou, China; Jiabao.AN20@student.xjtlu.edu.cn (J.A.); Luyao.Guo22@student.xjtlu.edu.cn (L.G.); Junjia.Zou18@student.xjtlu.edu.cn (J.Z.); Keliang.Zhang19@student.xjtlu.edu.cn (K.Z.); Yiheng.Zhong21@student.xjtlu.edu.cn (Z.Y.); Taimingwang.Liu20@student.xjtlu.edu.cn (T.L.); Long.Huang@xjtlu.edu.cn (L.H.) yi.chen02@xjtlu.edu.cn (Y.C.)

* Correspondence: yi.chen02@xjtlu.edu.cn

† These authors contributed equally to this work.

Abstract: Laser Powder Bed Fusion (L-PBF)-based manufacturing is a growing area of research, with a particular focus on evaluating constraints in printed products. This research emphasises the importance of considering various factors—including mechanical properties and support structures—that influence the final product during the design phase. Specifically, the design of microchannel heat exchangers is highlighted, where all constraints are critical. This article will present a method for analysing channel pressure limitations and report findings about mechanical properties loss from examining tube porosity. This includes a summary of results and the establishment of an experimental device system.

Keywords: laser powder bed fusion (L-PBF); microchannel heat exchangers; channel pressure capacity; tube porosity; experimental design

1. Introduction

1.1. Motivation, Aims and Objective

Advanced manufacturing represents the forefront of modern industrial processes, incorporating innovative technologies and methodologies to enhance production efficiency, product quality, and overall competitiveness. This paradigm shift from traditional manufacturing techniques is driven by the integration of digitisation, automation, and smart technologies [1]. Advanced manufacturing encompasses a range of cutting-edge practices, including the Internet of Things, artificial intelligence, robotics, and advanced materials, all of which contribute to creating more flexible, efficient, and sustainable manufacturing systems [2]. Among the various advanced manufacturing techniques, additive manufacturing, commonly known as 3D printing, has emerged as a transformative approach. Additive manufacturing involves the layer-by-layer construction of three-dimensional objects from digital models, enabling the creation of complex geometries that are often impossible or impractical to achieve with conventional subtracting methods. This technology offers numerous advantages, such as reduced material waste, shorter production times, and the ability to customise products to meet specific requirements. The significance of additive manufacturing extends across multiple industries, including aerospace, automotive, healthcare, and consumer goods. Its ability to produce lightweight, high-strength components with intricate designs has made it an essential tool for innovation and product development. Furthermore, additive manufacturing allows for rapid prototyping and on-demand production, which can significantly reduce lead times and costs associated with traditional manufacturing processes. In recent years, advancements in additive manufacturing technologies, such as Laser Powder Bed Fusion (L-PBF), have further expanded the potential applications of this method [3,4]. L-PBF utilises high-power lasers to selectively melt and fuse powdered materials, layer by layer, to create precise and high-performance parts. This process is particularly valuable for producing components with complex geometries and high mechanical requirements.

 doi:10.20944/preprints202407.1410.v1

The key advantage of L-PBF lies in its ability to produce components with complex internal channels and fine features, allowing for enhanced surface area-to-volume ratios and more efficient heat exchange. Precise control over material deposition facilitates the optimisation of channel dimensions and shapes, improving thermal performance. This flexibility allows for rapid prototyping and iterative testing, enabling engineers to quickly produce and evaluate multiple design variations, accelerating development and leading to innovative heat exchanger solutions. The Laser–Powder Bed Fusion (L-PBF) technique introduces a novel approach to constructing Microchannel Heat Exchangers (MCHX) for air conditioners. MCHX are highly versatile and can be applied across a wide range of industries due to their superior thermal performance and compact design. In the automotive industry, MCHXs are used in vehicle radiators, intercoolers, and air conditioning systems to improve cooling efficiency and reduce fuel consumption. In the aerospace sector, their lightweight and efficient heat transfer capabilities are crucial for thermal management in aircraft and spacecraft, where space and weight constraints are critical. The heating, ventilation, and air conditioning industry also benefits from MCHXs, as they enhance the energy efficiency of heating and cooling systems in residential, commercial, and industrial buildings [5,6]. In the electronics industry, MCHXs dissipate heat from high-performance computing systems and power electronics, ensuring reliable operation and extending the lifespan of components. Additionally, MCHXs are utilised in renewable energy systems, such as solar thermal collectors and geothermal heat pumps, to maximise energy capture and utilisation. Their ability to handle high pressures and temperatures makes them suitable for use in chemical processing and refrigeration industries as well. If L-PBF printed MCHXs are well developed, they could significantly advance all these industries by enabling the production of highly efficient, customised heat exchangers with complex geometries that are not feasible with traditional manufacturing methods. This would lead to improved thermal management solutions, increased energy efficiency, and enhanced performance across various applications, driving innovation and growth in multiple sectors. However, L-PBF faces several constraints and limitations in this area. For example, structures printed using L-PBF often exhibit significant defects that affect their mechanical properties and deformation behaviour [7]. Specifically, L-PBF-fabricated structures tend to have higher porosity levels compared to those produced by traditional manufacturing methods [8,9]. This increased porosity can negatively impact the mechanical properties of the printed objects, resulting in reduced structural integrity [10]. The porosity within the printed structures, which is a common defect arising from the L-PBF process, can make the material less dense and more porous than traditionally manufactured components. This can affect the material's strength and its ability to withstand pressure without leaking. When utilising ordinary Microchannel Heat Exchangers (MCHX), it is imperative to assess the pressure capacity of the channels before considering any enhancement treatments. Conducting burst tests is a fundamental process for ensuring compliance with safety standards [11]. Burst or blasting experiments are commonly used to measure the pressure capacity of traditionally manufactured microchannel heat exchangers, particularly in high-pressure applications such as refrigeration systems, where the refrigerant undergoes phase changes and may subject the channels to extremely high-pressure conditions [12,13]. Thorough testing of the pressure capacity of these microchannels is essential because failure due to inadequate pressure tolerance could result in catastrophic consequences. However, performing these experiments on PBF-printed MCHXs may not be suitable due to equipment limitations and the variable properties of the materials involved. Currently, there are limited experimental methodologies available for evaluating the pressure capacity of L-PBF-printed MCHXs.

Considering the potential defects associated with PBF-produced MCHXs, conducting burst tests may not always be necessary. Instead, prioritizing the development of reliable leakage measurement techniques could prove more beneficial. This approach would enable the accurate identification and evaluation of leakages, leading to more targeted and effective solutions for ensuring the integrity of MCHXs. Consequently, developing a straightforward experimental method to measure the pressure capacity of PBF-printed MCHXs is crucial. This would facilitate a comprehensive understanding of their performance and ensure that they meet the required standards for their intended applications.

 doi:10.20944/preprints202407.1410.v1

2. Literature Review

2.1. Introduction to MCHX

The Multi-Port Extrusion Tube (MPE Tube), also referred to as the Acer microchannel aluminum flat tube or microchannel tube, is a highly refined product known for its beneficial properties. These properties include low energy consumption, high performance, minimal space and weight requirements, and excellent resistance to corrosion and pressure [14]. Moreover, the MPE Tube offers high recycling value, reduced pressure drops, and quiet operation with a low refrigerant fill requirement. In addition to these performance benefits, an all-aluminium brazed heat exchanger using the MPE tube also shows enhanced corrosion resistance. This type of heat exchanger, featuring microchannels, is referred to as MCHX. MPE tubes are primarily used in applications such as condensers, evaporators, and heater cores. Figure 1 illustrates a simple appearance of this MCHX, highlighting its height, length, and width. The key components shown include the header, plate tube with microchannels, and louvred fin.

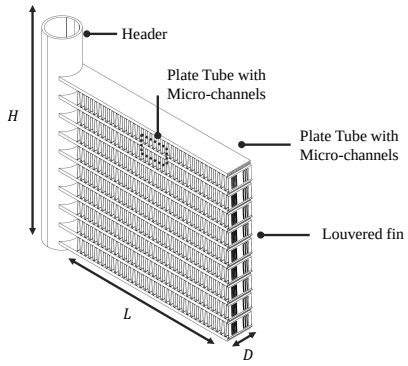

Figure 1. A simple showcase of the MCHX. Key components include the header, plate tubes with microchannels, and louvred fins. The diagram highlights the height (H), length (L), and width (D) dimensions of the MCHX, providing a clear view of its configuration and essential elements.

2.2. Introduction to L-PBF

Laser Powder Bed Fusion (L-PBF) represents a sophisticated additive manufacturing technique that employs high-power lasers to selectively melt and fuse powdered materials in a layer-by-layer manner, enabling the creation of intricate and high-precision components. This process is notable for its capability to produce parts with complex geometries that are often challenging or unfeasible to achieve using traditional manufacturing methods [15–17]. L-PBF is predominantly used for metals and alloys, making it especially valuable in sectors such as aerospace, medical devices, and mass and heat transfer, where there is a significant demand for customized, lightweight, and high-strength components.

Powder Bed Fusion (PBF) techniques, including those utilising lasers or electron beams, melt and fuse powder materials to fabricate parts. Electron Beam Melting (EBM), which operates in a vacuum, is specifically used for metals and alloys to produce functional components. In all PBF methods, a device such as a roller or a blade spreads the powder over previous layers. Fresh powder is supplied from a hopper or reservoir adjacent to the build platform. Figure 2 illustrates a basic working principle of L-PBF. In the PBF process, a thin layer of material, typically around 0.1 mm thick, is initially spread over the build platform. A laser then fuses the first layer or cross-section of the model. Following this, a new layer of powder is spread over the previous one using a roller. The laser continues to fuse subsequent layers or cross-sections, building the model layer by layer. This process repeats until the entire model is completed. Throughout the procedure, loose, infused powder remains in place around the model, which is later removed during post-processing to reveal the finished product.

 doi:10.20944/preprints202407.1410.v1

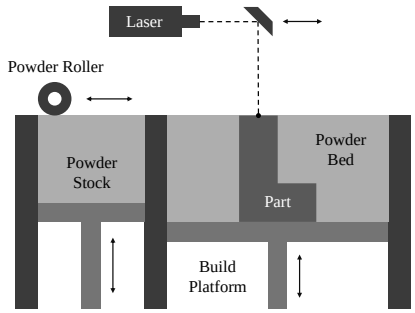

Figure 2. A simple showcase of the MCHX. Key components include the header, plate tubes with microchannels, and louvered fins. The diagram highlights the height (H), length (L), and width (D) dimensions of the MCHX, providing a clear view of its configuration and essential elements.

2.3. Introduction to Powder Material AlSi10Mg Properties

The AlSi10Mg alloy is commonly used in Additive Layer Manufacturing (ALM) and requires an understanding of its fatigue properties [18]. Parts made with ALM often have reduced structural integrity, making it crucial to evaluate material properties for applications like Heat Exchangers (MCHX). Factors such as orientation, platform temperature, post-process heating, and designation affect metal tensile stress. Zhang's experiment on tensile stress revealed that the printing direction significantly influences material properties [19]. Table 1 shows device settings and test results. The tensile strength of approximately 509 MPa is lower than that of forged samples, likely due to microscopic defects and non-uniform shapes in L-PBF parts, which also exhibit an elastic modulus of about 73 GPa, half that of forged samples. Kempen's research highlights that the orientation of samples can affect the outcomes of uni-axial tensile tests [18]. According to Kempen's findings, achieving the theoretical bulk density of 2.68 g/cm^3 for the material poses significant challenges. Although certain adjustments can allow an approximation of 99.8% of this theoretical density, the tensile strength of AlSi10Mg alloy produced via PBF is generally lower compared to that of cast products.

The mechanical properties of structures produced using L-PBF techniques are often lower compared to those fabricated through traditional methods. This reduction in mechanical performance is closely linked to the printing settings and various critical parameters, such as laser power, scanning speed, and material composition. Given these dependencies, it is crucial to develop an effective evaluation method for assessing the mechanical properties of PBF-printed parts. Such a method will help ensure that the printed components meet the required standards for their intended applications, providing a comprehensive understanding of their structural integrity and performance capabilities. The presence of porosity in Laser Powder Bed Fusion (L-PBF) printed Microchannel Heat Exchangers (MCHX) can adversely affect their mechanical properties and diminish their heat transfer efficiency [21]. In additive manufacturing, porosity appears in specific shapes, each associated with different mechanisms inherent to the additive process used. The formation of porosity in L-PBF is primarily influenced by process parameters [22]. Porosity reduces the load-bearing area, thereby serving as a potential initiation point for cracks. Nevertheless, minor porosity levels in L-PBF, even approaching 1%, do not substantially compromise the static strength of components [23]. However, this increased porosity can lead to reduced pressure capacity and a heightened risk of leakage within the tube channels. Given that MCHXs in air conditioners require high-pressure capacities [24], it is essential to accurately assess both the maximum pressure capacity and the incidence of any leakage events to ensure their reliability and performance.

 doi:10.20944/preprints202407.1410.v1

Table 1. Zhang's Experiment Setting and Testing Result.

Parameter	Value
Orientation	90° micro-rod (Parallel to the vertical direction)
Laser Power	190 W
Scanning Speed	900 mm/s
Displacement Rate	0.1 mm/min
Tensile Strength	509 MPa (approx.)
Test Result	Elastic modulus in 73 GPa (50% of forged samples)

3. Experiment Design and Methodology

3.1. Experiment Workflow

The primary objective of this experiment is to understand how porosity negatively impacts the pressure capacity of L-PBF printed tubes and to identify the factors that influence this pressure capacity. The experiment involves two main steps: "Experiment Tubes" and "Parameter Setting." Focusing on L-PBF printed tubes with varying porosity levels, the study examines their structural integrity under pressure to determine how porosity affects their pressure capacity. Both simulation in software and pressure testing device design are employed to achieve this goal. The simulation phase involves creating detailed models of the experiment tubes using software tools to predict the "Von Mises stress" and "Safety Factor" values, which are crucial for understanding the theoretical pressure capacity of the tubes. The "Von Mises stress" indicates the equivalent stress that combines the effects of normal and shear stresses, while the "Safety Factor" provides a margin of safety by comparing the material's yield strength to the applied stress. The pressure testing device applies controlled pressure to the tubes and observes the resulting structural behaviour, with bubble formation indicating leakage and structural failure. This empirical testing validates the simulation results and provides a comprehensive understanding of the tubes' pressure capacity. The theoretical pressure capacity evaluation involves comparing the simulation results with the experimental observations from the pressure testing device. By analysing the bubble formation phenomenon, the study correlates the theoretical predictions with the actual performance of the tubes under pressure. This comprehensive approach helps to understand the overall property of L-PBF printed tubes' pressure capacity and the extent to which porosity impacts their structural integrity, providing valuable insights into improving the design and manufacturing of more robust and reliable L-PBF printed components. The workflow of the overall experiment plan in displayed in Figure 3.

 doi:10.20944/preprints202407.1410.v1

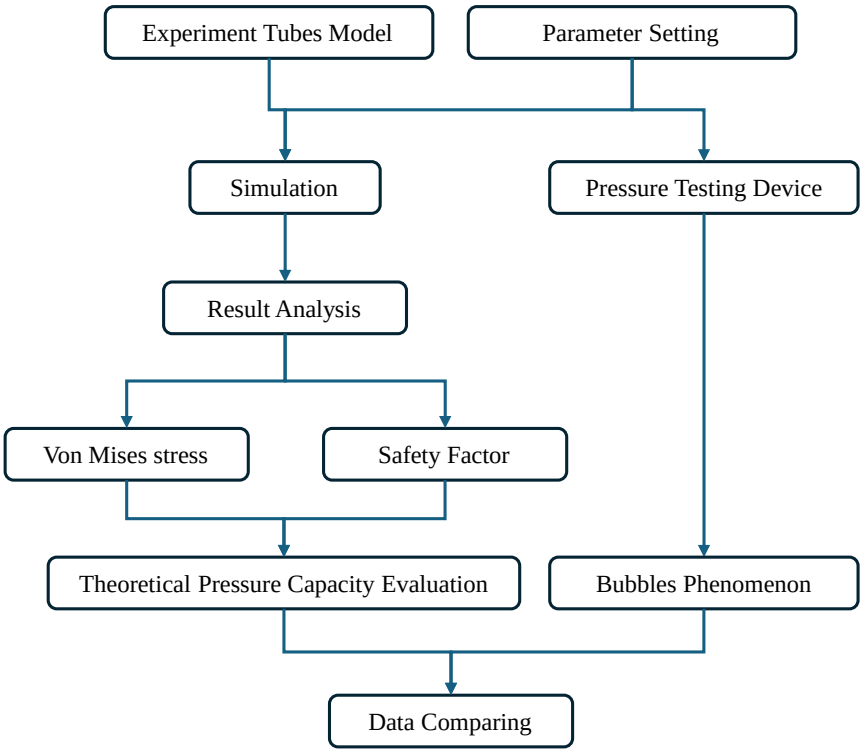

Figure 3. Experiment workflow illustration.

3.2. Simulation to Reflect the Pressure Capacity in Microchannel Tube

Before designing devices and equipment to evaluate the pressure capacity of L-PBF printed microchannels, it is crucial to understand the theoretical pressure values, potential pressure distribution, and the factors influencing pressure capacity. This foundational knowledge provides a benchmark for experimental evaluations and ensures accuracy in simulating real-world conditions. Understanding pressure distribution helps identify stress concentrations and potential failure points, informing the design of effective testing protocols. Additionally, recognizing the influence of wall thickness and material properties will be considered here, as these factors significantly impact the microchannels' performance under pressure. A thorough comprehension of these aspects enables the development of precise and reliable evaluation methods, ultimately ensuring the production of robust and dependable microchannel heat exchangers.

To establish a theoretical foundation for the experiment, research was conducted on the simulation process for the pressurized leakage detection experiment. Autodesk Inventor will be used for finite element analysis to understand the pressure distribution within the pipeline and to determine the associated safety coefficients. The material properties of AlSi10Mg, required for setting simulation parameters, are detailed in Table 2 [26–28]. This data table outlines the key properties of AlSi10Mg, highlighting its suitability for structural applications. AlSi10Mg has a thermal conductivity of 163 W/m·K and a specific heat of 0.730 J/g·°C, which ensures efficient heat management. Its thermal expansion coefficient of 21.800 µm/m·°C provides dimensional stability under temperature variations. Mechanically, AlSi10Mg exhibits a Young's modulus of 54.500 GPa, a Poisson's ratio of 0.25, and a shear modulus of 20.960 MPa, indicating good stiffness and shear resistance. With a density of 2.640 g/cm^3, it is ideal for lightweight applications. The material's yield strength is 102.100 MPa and its tensile strength is 296.000 MPa, demonstrating its capacity to withstand significant stress. These attributes make AlSi10Mg a reliable choice for automotive and aerospace applications, where both thermal management and mechanical integrity are crucial.

 doi:10.20944/preprints202407.1410.v1

Table 2. Physical Properties of AlSi10Mg.

Tag	Value
Behavior	Iso
Thermal Conductivity	1.630E+02 W/m·K
Specific Heat	0.730 J/g·°C
Thermal Expansion Coefficient	21.800 µm/m·°C
Young's Modulus	54.500 GPa
Poisson's Ratio	0.25
Shear Modulus	20.960 MPa
Density	2.640 g/cm³
Damping Coefficient	0.002(0)
Yield Strength	102.100 MPa
Tensile Strength	296.000 MPa

Before commencing the simulation, it is necessary to establish specific preparatory settings. The dimensions of the tube, especially its length, should correspond to those of the experimental test sample to ensure consistency. It is important to note that simulation outcomes may not entirely reflect actual results due to inherent modelling limitations. Autodesk Inventor's stress simulation interface is optimised for solid structures, which may impact accuracy. Nonetheless, it is capable of effectively illustrating pressure distribution and stress characteristics on the pipe's surface, offering valuable insights. Figure 4 presents the simulation model with a transparent three-quarter section view.

$$\text{Safe Stress} = \frac{\text{Yield Strength}}{\text{Safety Factor}} \tag{1}$$

In equation 1:

- **Safe Stress** is the maximum allowable stress that ensures the component will perform reliably under expected loads.
- **Yield Strength** is the stress at which the material begins to yield or deform elastically.
- **Safety Factor** is a multiplier used to provide a margin of safety, typically greater than 1, to account for uncertainties and variability in the material and loading conditions.

Von Mises stress and safety factors serve as key references to represent the tube's performance in the simulation, ensuring alignment with the experimental scheme. The "safe stress" for AlSi10Mg or any structural component is derived from its yield strength by applying a safety factor [29,30], as outlined in Equation 1. Safe stress is a calculated value used in engineering to ensure that a material or structural component can withstand the applied loads without failure. It is determined by dividing the yield strength of the material by a safety factor. The yield strength is the stress at which a material begins to deform elastically and is no longer able to return to its original shape. The safety factor is a dimensionless number that provides a margin of safety to account for uncertainties in the material properties, loading conditions, and potential imperfections in the material or design.

Geometric discontinuities such as sharp bends or holes can cause stress concentrations, leading to localised increases in stress. The von Mises stress calculation, shown in Equation 2, combines principal stresses from all three orthogonal axes, providing a scalar value that represents the combined effect of normal and shear stresses. The von Mises stress, σ_{vm}, is a theoretical construct used in engineering to predict the yielding of materials under complex loading conditions. It is especially useful in the

 doi:10.20944/preprints202407.1410.v1

field of structural and mechanical engineering because it helps determine whether a given material will yield (begin to deform elastically) under a given set of stresses. This method can indicate elevated stress levels beyond those directly applied. Here, σ_1, σ_2, and σ_3 denote the principal stresses.

$$\sigma_{vm} = \sqrt{\frac{(\sigma_1 - \sigma_2)^2 + (\sigma_2 - \sigma_3)^2 + (\sigma_3 - \sigma_1)^2}{2}} \quad (2)$$

In equation 12:

- σ_{vm} is the von Mises stress.
- σ_1, σ_2, **and** σ_3 are the principal stresses

Uniformly applied pressure may not produce a uniform stress state within the material, often resulting in elevated von Mises stresses. Complex loading conditions, such as bending and torsional stresses, significantly contribute to this phenomenon. Additionally, material inhomogeneities, such as anisotropy or internal voids, and specific boundary conditions during testing can further increase stress readings [31,32]. Detailed computational analysis, such as finite element analysis (FEA), is crucial for visualizing these stress distributions, optimizing design, and ensuring both safety and functionality.

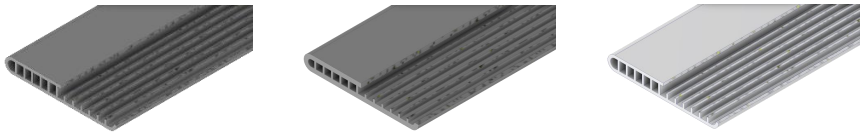

(a) (b) (c)

Figure 4. Transparent three-quarter section view. (**a**) 1.0x AlSi10Mg tube with a wall thickness of 0.35mm. (**b**) 1.5x AlSi10Mg tube with a wall thickness of 0.53mm. (**c**) 1.0x aluminium tube with a wall thickness of 0.35mm.

3.3. Simulation Result

Figure 5 and Figure 6 illustrates the simulation results for von Mises stress and safety factors of three tubes (1.0x Tube, 1.5x Tube, and 1.0x Aluminium Tube) subjected to pressures ranging from 2 MPa to 12 MPa. For the 1.0x Tube, the maximum von Mises stress increases linearly, exceeding the 40 MPa safety threshold above 6 MPa, with the minimum safety factor decreasing from 14.12 at 2 MPa to 1.96 at 12 MPa. This reduction indicates a shrinking safety margin and a higher risk of failure at elevated pressures. The intersection of the calculated safety factor with the constant safety line around 4 MPa signifies a critical transition point, beyond which the actual safety factor falls below the threshold of 3.

The 1.5x Tube exhibits a similar pattern, with maximum stress rising from 8.65 MPa at 2 MPa to 51.93 MPa at 12 MPa, surpassing the safety threshold above 4 MPa, and the minimum safety factor dropping from 13.98 to 2.33. Conversely, preliminary experimental evaluations showed a significant divergence in the performance of the 1.0x Tube from the simulated outcomes. Initial testing revealed that the 1.0x Tube began leaking at a constant pressure of 1 MPa, whereas simulations did not predict leakage until pressures between 8 MPa and 10 MPa. This discrepancy highlights the challenges in accurately replicating real-world behaviours in simulations, emphasising the need to calibrate simulation models based on empirical data to improve predictive accuracy and reliability.

The 1.0x Aluminium Tube demonstrates better performance, with maximum stress increasing from 8.716 MPa at 2 MPa to 52.29 MPa at 12 MPa, remaining below the 91.67 MPa safety level, and the minimum safety factor decreasing from 15 to 5.26. The comprehensive simulation, extending up to a pressure of 12 MPa, allows for a thorough analysis of mechanical properties under varying conditions,

 doi:10.20944/preprints202407.1410.v1

enhancing the understanding of material behaviour and structural integrity under increased loads. These results suggest that the aluminium tube has a superior safety margin and a lower risk of damage compared to the AlSi10Mg printed tubes under similar pressure conditions.

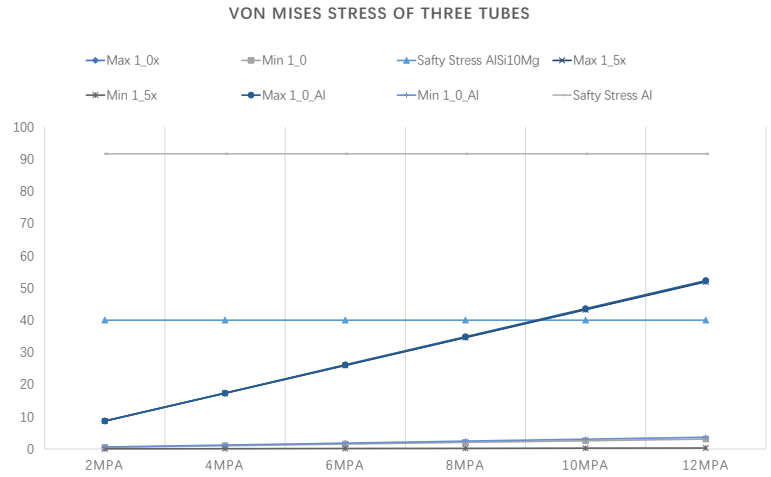

Figure 5. Simulation results for von Mises stress of three tubes.

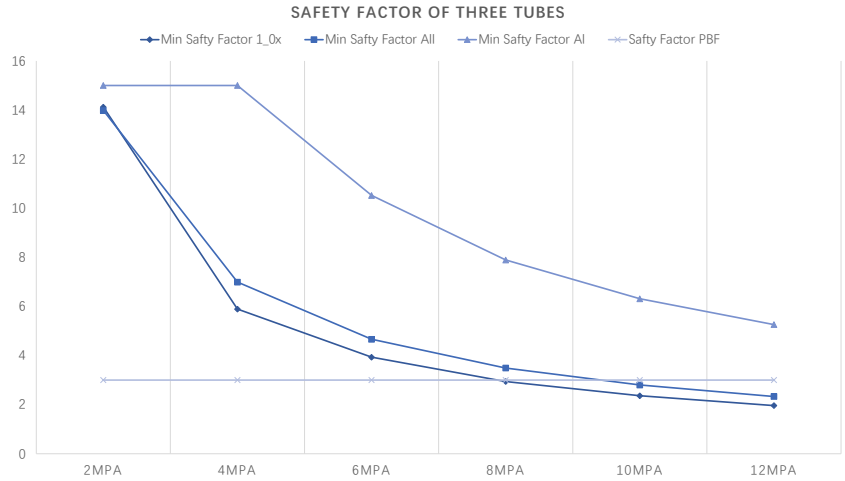

Figure 6. Simulation results for safety factors of three tubes.

Although the simulation results indicate that L-PBF printed products have poorer mechanical properties compared to aluminium tubes, it is important to recognise that these simulations often assume the product is virtually free of porosity. This means that the actually printed tubes, which are likely to contain some level of porosity, may exhibit even poorer properties in terms of von Mises stress and safety factors. Consequently, the real-world performance of L-PBF printed tubes could be significantly compromised, further emphasising the need for empirical testing and model calibration to accurately reflect the material's true behaviour under operational conditions.

According to Figure 7 and Figure 8, larger pressure distribution areas are predominantly found on the inner walls of the tubes. Additionally, the outer surface of the tubes also shows notable pressure distribution, although to a lesser extent than the inner walls. When comparing the tubes, the 1.5x wall thickness tube exhibits a better pressure-holding capacity, as indicated by a more uniform and lower stress distribution compared to the 1.0x Tube. This suggests that increasing the wall thickness enhances the tube's ability to withstand higher pressures. In contrast, the 1.0x wall thickness tube shows a more fragile structure overall, as evidenced by the higher von Mises stresses. The 1.0x

 doi:10.20944/preprints202407.1410.v1

Aluminium Tube demonstrates superior performance, with maximum stress levels significantly below the safety threshold, indicating a more stable and reliable structure. This tube also exhibits similar pressure distribution characteristics to the L-PBF printed tubes but with better pressure-holding effects. Moreover, the distribution of the safety factor similarly shows that the 1.0x wall thickness tubes exhibit a more fragile structure overall. However, the 1.5x wall thickness tubes, despite being made from the same material, exhibit a more stable state. Regardless of the wall thickness, the 1.0x aluminium tube is structurally more stable and reliable compared to the L-PBF printed tubes.

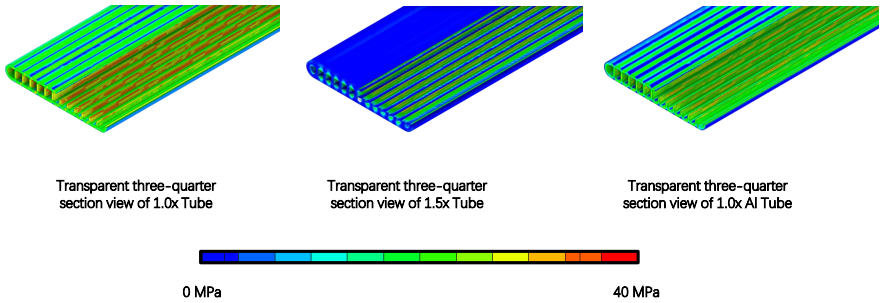

Figure 7. The diagram illustrates the von Mises stress distribution on three tubes under a channel pressure of 8 MPa. The tubes shown are the 1.0x Tube, the 1.5x Tube, and the 1.0x Aluminium Tube, each displayed in a transparent three-quarter section view.

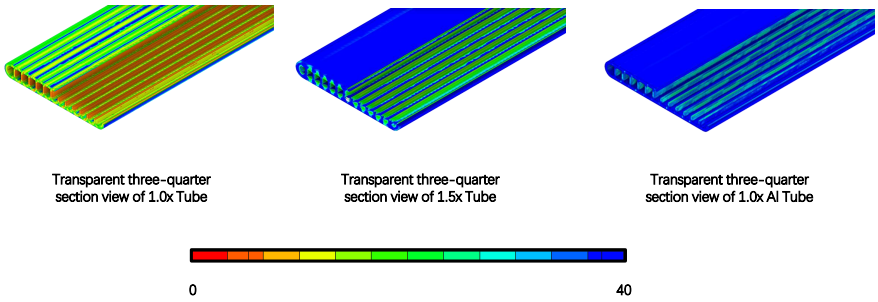

Figure 8. The diagram illustrates the safty factor distribution on three tubes under a channel pressure of 8 MPa. The tubes shown are the 1.0x Tube, the 1.5x Tube, and the 1.0x Aluminium Tube, each displayed in a transparent three-quarter section view.

4. Pressure Capacity Testing Experiment

4.1. Experiment Device Preparation

To secure the PBF printed tube for testing and apply a specific air pressure, a pressure testing unit (PTD) is placed inside an acrylic tank (AT). Two end caps are used to ensure an airtight seal. One end cap includes an optional pressure gauge for monitoring, while the other is connected to a nitrogen supply to introduce the pressure. The experiment involves two types of PBF printed tubes with identical width and thickness but differing wall thicknesses. The objective is to determine the impact of porosity on structural integrity by identifying the pressure at which leakage begins, indicating structural failure. Figure 9 depicts the experimental setup. Nitrogen is used as the pressurisation agent to simulate the dynamic pressure environment of gaseous refrigerants within microchannels. The setup, including the tube, is placed within an acrylic tank, which is then filled with water to a level above the tube to facilitate the observation of air leakage under pressure. The experiment evaluates the structural integrity of L-PBF printed microchannel under varying pressures. A gradient pressure test is conducted, starting at 1 MPa for 10 minutes. If no changes occur, the pressure is increased by 0.2 MPa increments until 2 MPa. Photographic documentation at each increment will monitor bubble formation, indicating the pressure point of leakage and quantifying the sample's pressure

 doi:10.20944/preprints202407.1410.v1

endurance. The setup features a barometric system equipped with a pressure gauge and a variable pressure regulator to ensure precise pressure control. High-definition video recording equipment is used to document the external conditions of the tube, capturing periodic photographs for time-series analysis of any leakage.

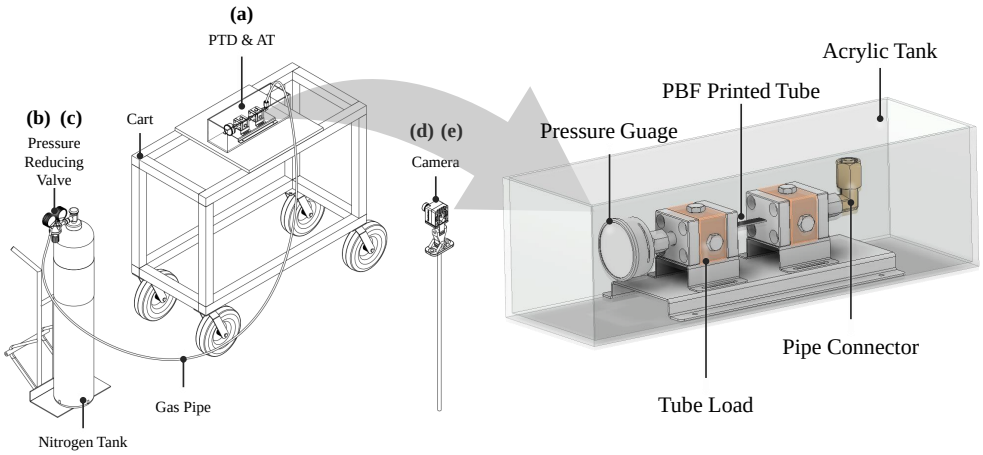

Figure 9. Experimental Procedure: (**a**) Initial Setup: Prepare the experimental setup by ensuring the nitrogen gas supply and pressure regulating equipment are properly configured and connected to the sample; (**b**) Baseline Measurement: Apply an initial pressure of 1 MPa to the sample and maintain it for 10 minutes to establish a baseline for the tube's condition; (**c**) Incremental Pressure Application: Gradually increase the pressure in 0.2 MPa increments, maintaining each pressure level for 10 minutes if no observable changes occur, continuing until a maximum pressure of 2 MPa is reached; (**d**) Monitoring and Documentation: At each pressure increment, utilize high-definition video and photography to document the tube's surface condition, specifically observing for bubble formation or any signs of leakage; (**e**) Data Analysis and Recording: Analyze the visual data collected to identify the pressure point at which leakage begins, recording the findings for further analysis regarding the tube's pressure endurance and structural integrity.

4.2. Experiment Method of Bubbles Phenomenon

To enhance the analysis of observed phenomena and their causes, the bubble formations documented in the three experiments have been categorised into four distinct types as illustrated in Figure 10. These categories are defined as follows: 'nearly no bubbles', 'micro and attached bubbles', 'micro and small bubbles', and 'numerous and violent'. This classification allows for a systematic review of the data and facilitates a clearer understanding of the underlying dynamics at each stage of the experiment. The primary objective of this experiment is to investigate the impact of wall thickness on the pressure capacity of PBF printed tubes. By visualising the phenomenon of bubble leakage, the ability of these tubes to withstand specific pressure conditions can be evaluated. The experiment involves incrementally increasing the internal pressure of the tubes and observing the formation of bubbles as an indicator of leakage. This visual method provides a practical means of assessing the structural integrity and pressure-bearing capacity of tubes with varying wall thicknesses. The critical pressure points at which structural failure occurs will be identified, offering valuable insights into the performance and reliability of PBF printed tubes under different pressure conditions. This approach enhances the understanding of the relationship between wall thickness and pressure capacity, contributing to the development of more robust and reliable PBF printed components.

 doi:10.20944/preprints202407.1410.v1

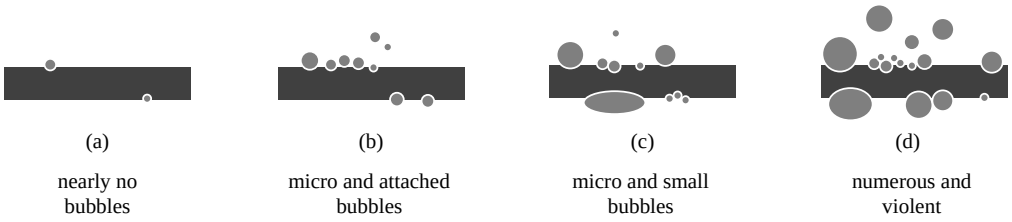

Figure 10. Bubble Status: **(a)** 'nearly no bubbles,' where the pressure is insufficient to compromise the tube's structural integrity, possibly due to dissolved air or micro-perforations in the tube; **(b)** 'micro and attached bubbles,' where larger bubbles are present and adhere to the tube surface along with persistent micro bubbles; **(c)** 'micro and small bubbles,' where some micro bubbles grow into small bubbles that primarily remain attached to the tube surface, with clusters forming underneath; and **(d)** 'numerous and violent,' characterized by a rapid increase in both the number and detachment rate of bubbles, with significant clustering observed on the lower surface.

Porosity and void formation within the fabricated microstructure are critical factors affecting the integrity and mechanical properties of components produced via L-PBF. Figure 11 illustrates the spatial distribution of these voids, which appear as darkened spots or gaps within the solid matrix. These discontinuities often result from suboptimal melting or consolidation of powder particles during the PBF process. Contributing factors may include inconsistent energy input from the laser, variations in powder layer thickness, or thermal gradients leading to uneven solidification rates. The morphology and distribution of these porosities significantly influence the mechanical performance of the material, as they can act as stress concentrators and initiation points for crack propagation under load. Additionally, porosity is a direct cause of leakage and bubble formation during pressurization tests. The presence of voids and gaps creates pathways for gas to escape, resulting in the observed leakage and bubble phenomena. These porosity holes also weaken the structural integrity of the tube, making it more susceptible to failure under gas pressure.

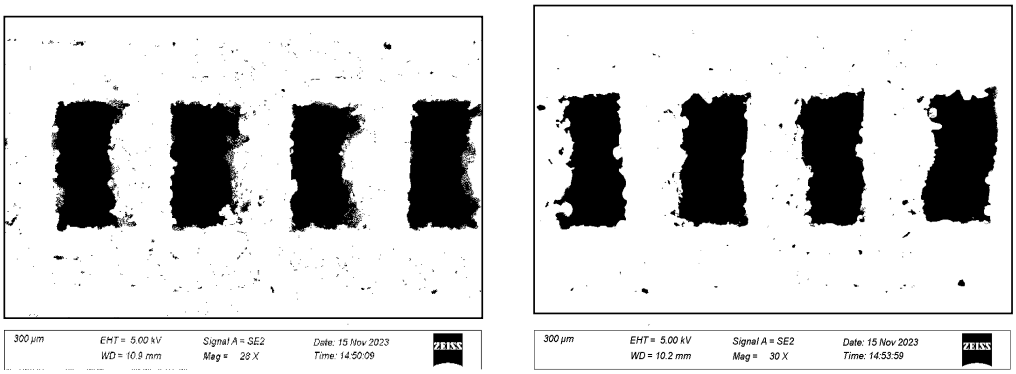

Figure 11. Cross-sectional area showing the porosity distribution in one of the L-PBF printed tubes with a 1.0x wall thickness.

4.3. Tube Pressure Capacity Testing Experiment Result

The experiment 1 evaluates the pressure capacity of a tube with a 1.0x wall thickness over a duration of 1 hour, recording the pressure every 10 minutes. Beginning at 1.0 MPa, the pressure is incrementally increased by 0.2 MPa at each interval. Table 3 illustrates the pressure capacity assessment of a tube with a 1.0x wall thickness over a duration of 1 hour, starting at 1.0 MPa and increasing by 0.2 MPa every 10 minutes. At 1.0 MPa, leakage was observed at 34 seconds, with numerous violent bubbles on the upper surface and larger bubbles forming on the lower surface. At 1.2 MPa, the leakage patterns remained consistent. At 1.4 MPa, the rate of bubble overflow increased. At 1.6 MPa, no significant changes were detected. At 1.8 MPa, new leakage areas emerged, indicating

 doi:10.20944/preprints202407.1410.v1

potential structural weaknesses, and a significant increase in bubble overflow was noted, highlighting progressive structural degradation under sustained high pressure.

Table 3. 1.0x Tube Pressure Performance-Experiment 1.

Stage	Pressure Gauge Value	Time Step	Important Time Step	Leakage Level	Bubbles Performance
Stage 1	1.0 MPa	0s	0min 34s	medium	numerous and violent
Stage 2	1.2 MPa	10min	-	high	numerous and violent
Stage 3	1.4 MPa	20min	-	high	numerous and violent
Stage 4	1.6 MPa	30min	-	extreme	numerous and violent
Stage 5	1.8 MPa	40min	-	extreme	numerous and violent
Stage 6	2.0 MPa	60min	-	extreme	numerous and violent

For the 1.5x tube, the experiment 2 involved incremental pressure increases with observations at 10-minute intervals, as shown in Table 4. At 1.0 MPa, minimal bubble activity was observed. At 1.2 MPa, small bubbles adhered to the surface, with a few detaching after 10 minutes. At 1.4 MPa, small bubbles began to slowly emerge after 20 minutes. At 1.6 MPa, the emission rate of small bubbles increased. At 1.8 MPa and 2.0 MPa, the leakage patterns remained consistent, but the formation and release rate of small bubbles accelerated. This progression highlights the tube's response to increasing pressure, emphasizing changes in bubble activity and potential structural weaknesses.

Table 4. 1.5x Tube Pressure Performance-Experiment 2.

Stage	Pressure Gauge Value	Time Step	Important Time Step	Leakage Level	Bubbles Performance
Stage 1	1.0 MPa	0s	-	No	Nearly-No-Bubbles
Stage 2	1.2 MPa	10min	10min 23s	slight	micro and attached bubbles
Stage 3	1.4 MPa	20min	20min 12s	slight	micro and small bubbles
Stage 4	1.6 MPa	30min	-	low	micro and small bubbles
Stage 5	1.8 MPa	40min	-	low	micro and small bubbles
Stage 6	2.0 MPa	60min	-	low	micro and small bubbles

 doi:10.20944/preprints202407.1410.v1

To establish a benchmark and minimize non-essential influences, an aluminum tube was selected for comparison in Experiment 3. The conditions were identical to those in the previous two experiments, with the process lasting one hour and pressures recorded every 10 minutes. Starting at an initial pressure of 1.0 MPa, the pressure was increased by 0.2 MPa at regular intervals, as shown in Table 5. For the flat tube, negligible bubble activity was observed at 1.0 MPa during the first 10 minutes. Minimal bubble activity continued at 1.2 MPa. From 1.4 MPa to 1.8 MPa, the tube remained stable with no significant changes. At 2.0 MPa, small bubbles appeared, likely due to dissolved air in the water rather than a defect in the tube. This pattern indicates consistent stability across increasing pressure stages, with minimal bubble activity suggesting robust structural integrity.

Table 5. 1.0x Al Tube Pressure Performance-Experiment 3.

Stage	Pressure Gauge Value	Time Step	Important Time Step	Leakage Level	Bubbles Performance
Stage 1	1.0 MPa	0s	-	No	Nearly-No-Bubbles
Stage 2	1.2 MPa	10min	10min 23s	slight	micro and attached bubbles
Stage 3	1.4 MPa	20min	20min 12s	slight	micro and small bubbles
Stage 4	1.6 MPa	30min	-	low	micro and small bubbles
Stage 5	1.8 MPa	40min	-	low	micro and small bubbles
Stage 6	2.0 MPa	60min	-	low	micro and small bubbles

4.4. Tube Pressure Capacity Testing Experiment Result Evaluation

Figure 12 presents SEM images of the tube channels, illustrating that machined parts generally withstand greater pressures due to higher density, while PBF parts suffer from high porosity, compromising their pressure resistance. The cracks in the 1.0x tube facilitated gas leakage, with segments clumping and dislodging. The comprehensive results from this experimental study highlight porosity as the predominant factor influencing the pressure resistance capabilities of microchannels fabricated via Powder Bed Fusion (PBF) printing. Porosity negatively impacts the mechanical properties of materials, significantly reducing the structural integrity of PBF-printed components. This reduction in material properties is especially concerning for applications requiring high-pressure endurance. Several factors contribute to porosity development in PBF processes, including particle size distribution, energy input, scanning strategy, and atmospheric control during printing. Each of these elements can affect the density and mechanical strength of the final product. Empirical observations from the study also reveal that increasing the wall thickness of the microchannel tubes markedly enhances their ability to withstand pressurization. This is evidenced by the comparative analysis of the 1.5x Tube versus the 1.0x Tube. Although the 1.5x Tube exhibited minor air leakage in certain areas, its overall performance in pressurization tests was superior to that of the thinner-walled 1.0x Tube. This improvement underscores the critical role of wall thickness in mitigating the adverse effects of porosity and enhancing the functional reliability of PBF-printed microchannels under pressure.

 doi:10.20944/preprints202407.1410.v1

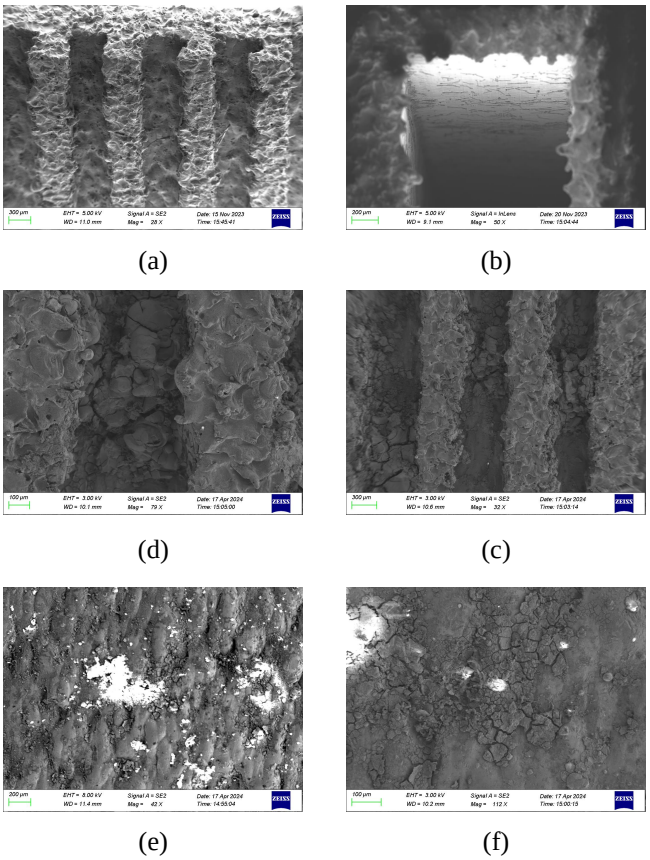

Figure 12. SEM images illustrating the channels: (a) Tubes that have not undergone pressure testing. (b) Machined tube channel surface. (c) Cracks in the inner tube channel (wide field view). (d) Cracks in the inner tube channel (focused view). (e) Cracks in the inner tube channel (wide field view). (f) Cracks in the inner tube channel (focused view).

5. Discussion

This experiment provides a preliminary method to evaluate the approximate pressure capacity of L-PBF printed tubes. However, some limitations and inaccuracies need to be addressed. The current approach requires further refinement and modification to achieve more precise and reliable results. The experiment was conducted with a limited number of specimens, and the variability in material properties and manufacturing parameters was not fully accounted for. Future studies should involve a larger sample size to better understand the statistical significance of the findings. Additionally, more comprehensive consideration of parameters such as laser power, scanning speed, layer thickness, and powder quality is essential to gain a deeper insight into their effects on porosity and pressure capacity. Despite these limitations, the experiment offers a straightforward and practical way to understand the impact of porosity on pressure capacity. The visualisation of bubble formation and leakage provides valuable information on the structural integrity of the tubes. While further improvements are necessary, this method lays the groundwork for future research and development, highlighting the critical role of porosity in determining the mechanical performance of L-PBF printed components. This initial study, though limited, serves as a stepping stone toward optimising the structural integrity of L-PBF printed tubes and enhancing their applicability in high-pressure environments.

6. Conclusions

The investigation presented in this dissertation has significantly advanced the understanding of porosity's impact on the pressure capacity of microchannel tubes manufactured using L-PBF. Central to this research was the examination of two types of PBF-printed tubes, identical in width

 doi:10.20944/preprints202407.1410.v1

and thickness but varying in wall thickness, to assess the impact of porosity on structural integrity by determining the pressure point at which leakage occurs, indicating structural failure. The experiments utilised nitrogen as the pressurisation agent, simulating the dynamic pressure environment typical of gaseous refrigerants in microchannels. The experimental setup included a barometric system with a pressure gauge and a variable pressure regulator to ensure precise modulation of pressure, accurately reflecting operational conditions. High-definition video recording and intervocalic photography were employed to meticulously document the tube conditions, allowing for detailed time-series analysis of leakage events. One of the key innovations in this research was the development and use of a novel experimental method and equipment to simulate and analyse the pressure conditions in L-PBF printed tubes, providing a robust framework for understanding the effects of porosity on pressure capacity. Additionally, the study explored the material properties of the AlSi10Mg alloy commonly used in these processes and found that printing parameters significantly influence the mechanical behaviour of this alloy, underscoring the necessity of controlling these parameters to mitigate inherent weaknesses such as porosity, which leads to reduced structural integrity and performance under pressure. A notable innovation was the identification of strategies such as increasing wall thickness as a potential indicator for enhancing the pressure-bearing capacity of PBF flat tubes, significantly improving the tubes' ability to withstand high pressures by increasing the material volume to absorb and distribute stress more effectively. Furthermore, the research provided clear definitions of four phenomena observed in pressure-bearing failure: negligible bubble activity, minimal bubble activity, increased bubble emission rate, and new leakage areas. These detailed observations are critical for developing more precise methods to quantify and understand the impact of porosity on structural integrity. In conclusion, this dissertation not only elucidates the critical role of structural design and precise experimental control in optimising the performance of PBF-manufactured MCHX but also underscores the complexity of managing and mitigating the effects of porosity. The findings from this study contribute substantially to the field of additive manufacturing, providing valuable insights and practical guidelines for designing and producing more reliable and efficient microchannel heat exchangers. These insights pave the way for further research aimed at overcoming the current limitations of PBF technology and enhancing its applicability in demanding industrial applications.

7. Future Works

The future work in advancing the understanding and application of L-PBF printed Microchannel Heat Exchangers (MCHXs) will focus on several key areas:

- Expanding Material Range: Future research will explore a broader range of materials beyond AlSi10Mg to determine if the observed effects of porosity on pressure capacity are consistent across different alloys and composite materials. This will help identify materials best suited for various industrial applications.
- Variety of Tube Geometries and Wall Thicknesses: Increasing the variety of tube geometries and wall thicknesses will provide a more comprehensive dataset. This will enable the identification of optimal designs for different use cases, enhancing the performance and efficiency of MCHXs.
- Refining Simulation Models: To improve the accuracy of predictions for "Von Mises stress" and "Safety Factor," future work will involve refining simulation models to incorporate more detailed material properties and advanced computational techniques. This includes considering thermal effects, residual stresses, and real-time monitoring of the printing process.
- In-situ Monitoring Techniques: Developing and implementing in-situ monitoring techniques during the L-PBF process will be crucial. Real-time sensors and data acquisition systems can detect and mitigate porosity and other defects as they occur, leading to higher quality prints and reduced post-processing requirements.
- Extensive Testing: Conducting more extensive testing under a wider range of pressure conditions and environmental factors is essential. This includes long-term durability tests under cyclic

 doi:10.20944/preprints202407.1410.v1

loading and thermal cycling to assess the performance of L-PBF printed tubes in real-world conditions.

- Quantifying Bubble Phenomenon: Developing a more precise method to quantify the bubble phenomenon during pressure testing. Accurate quantification of bubble formation and behavior will provide better insights into the structural integrity and pressure capacity of the printed tubes.

Author Contributions: Author contributions: Jiabao An: Conceptualization, Methodology, Writing—Review and Editing, Writing—Original Draft Preparation; Luyao Guo: Experiment assistant and device support; Yiheng Zhong & Taimingwang Liu: Investigation, Resources, Software; Junjia Zou & Keliang Zhang: Technical instructor; Long Huang: Supervision, Funding Acquisition; Yi Chen: Project Administration, Supervision. All authors have read and agreed to the published version of the manuscript

Funding: This work was supported by the XJTLU Research Development Fund (RDF-21-02-019). We would like to express our gratitude for this funding support, which has been instrumental in carrying out this research.

Data Availability Statement: The authors do not intend to share the data associated with this study. Data sharing is not applicable due to privacy and ethical considerations.

Acknowledgments: This work was supported by the Research Development Fund (RDF-21-02-019) and the School Research Priorities Seed Funding (SRPSF-2023-05)

Conflicts of Interest: The funders had no role in the design of the study; in the collection, analyses, or interpretation of data; in the writing of the manuscript; or in the decision to publish the results.

Abbreviations

The following abbreviations are used in this manuscript:

L-PBF	Laser Powder Bed Fusion
MCHX	Microchannel Heat Exchanger
PBF	Powder Bed Fusion
PTD	Pressure Testing Device
AT	Acrylic Tank
MPa	Megapascal
SEM	Scanning Electron Microscope

Appendix A

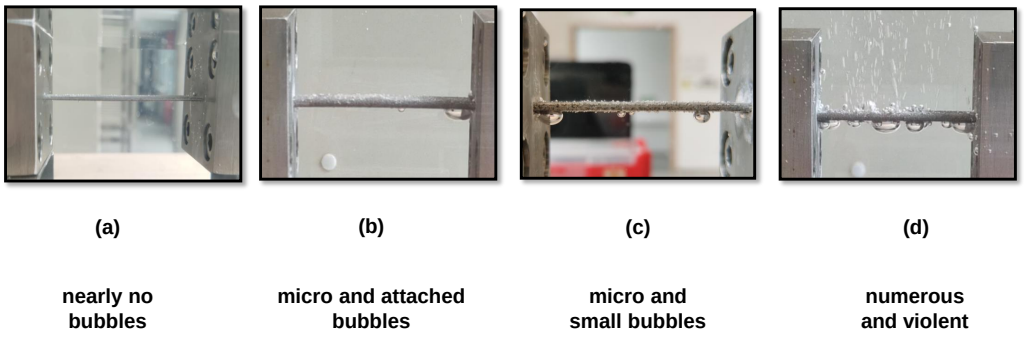

Figure A1. Bubble Status of real experiment process: **(a)** 'nearly no bubbles,' where the pressure is insufficient to compromise the tube's structural integrity, possibly due to dissolved air or micro-perforations in the tube; **(b)** 'micro and attached bubbles,' where larger bubbles are present and adhere to the tube surface along with persistent micro bubbles; **(c)** 'micro and small bubbles,' where some micro bubbles grow into small bubbles that primarily remain attached to the tube surface, with clusters forming underneath; and **(d)** 'numerous and violent,' characterized by a rapid increase in both the number and detachment rate of bubbles, with significant clustering observed on the lower surface.

 doi:10.20944/preprints202407.1410.v1

Figure A2. Showcase of real testing equipment.

References

1. Ashima, R.; Haleem, A.; Bahl, S.; Javaid, M.; Mahla, S. K.; Singh, S. Automation and manufacturing of smart materials in Additive Manufacturing technologies using Internet of Things towards the adoption of Industry 4.0. *Materials Today: Proceedings* **2021**, *45*, 5081–5088.
2. Wang, B.; Tao, F.; Fang, X.; Liu, C.; Liu, Y.; Freiheit, T. Smart manufacturing and intelligent manufacturing: A comparative review. *Engineering* **2021**, *7*(6), 738–757.
3. Gibson, I.; Rosen, D. W.; Stucker, B.; Khorasani, M. Additive manufacturing technologies. *Springer* **2021**, *17*.
4. Abdulhameed, O.; Al-Ahmari, A.; Ameen, W.; Mian, S. H. Additive manufacturing: Challenges, trends, and applications. *Advances in Mechanical Engineering* **2019**, *11*(2), 1687814018822880.
5. Hussain, A. R. J.; Alahyari, A. A.; Eastman, S. A.; Thibaud-Erkey, C.; Johnston, S.; Sobkowicz, M. J. Review of polymers for heat exchanger applications: Factors concerning thermal conductivity. *Applied Thermal Engineering* **2017**, *113*, 1118–1127.
6. Zahir, M. Z.; Ahmed, A.; Akhtar, K.; Mehmood, A. Microchannel Heat Exchanger (MCHX) for Waste Heat Recovery Using Water and Organic Fluid. *Journal of Applied and Emerging Sciences* **2023**, *13*(1), 67–75.
7. Lei, H.; Li, C.; Meng, J.; Zhou, H.; Liu, Y.; Zhang, X.; Wang, P.; Fang, D. Evaluation of compressive properties of SLM-fabricated multi-layer lattice structures by experimental test and μ-CT-based finite element analysis. *Materials & Design* **2019**, *169*, 107685.
8. Du Plessis, A. Porosity in laser powder bed fusion. In *Fundamentals of Laser Powder Bed Fusion of Metals*; Elsevier, 2021; pp. 155–178.
9. Morano, C.; Pagnotta, L. Additive manufactured parts produced by selective laser sintering technology: porosity formation mechanisms. *Journal of Polymer Engineering* **2023**, *43*(6), 537–555.
10. Stránský, O.; Beránek, L.; Pathak, S.; Kaufman, J.; Böhm, M.; Kopeček, J.; Holešovský, F.; Petrášek, Š.; Hlavňková, L.; Soukup, Z. Porosity and microstructure of L-PBF printed AlSi10Mg thin tubes in laser shock peening. *Journal of Materials Research and Technology* **2023**, *27*, 1683–1695.
11. Krishnaswamy, R. K. Analysis of ductile and brittle failures from creep rupture testing of high-density polyethylene (HDPE) pipes. *Polymer* **2005**, *46*(25), 11664–11672.
12. Kleinschmit, N. N. A shock tube technique for blast wave simulation and studies of flow structure interactions in shock tube blast experiments, 2011.
13. Kumar, R.; Nedungadi, A. Using gas-driven shock tubes to produce blast wave signatures. *Frontiers in Neurology* **2020**, *11*, 90.
14. Zou, J.; Hirokawa, T.; An, J.; Huang, L.; Camm, J. Recent advances in the applications of machine learning methods for heat exchanger modeling—a review. *Frontiers in Energy Research* **2023**, *11*, 1294531.

15. Chmielewska, A.; Wysocki, B.; Kwaśniak, P.; Kruszewski, M. J.; Michalski, B.; Zielińska, A.; Adamczyk-Cieślak, B.; Krawczyńska, A.; Buhagiar, J.; Święszkowski, W. Heat treatment of NiTi alloys fabricated using laser powder bed fusion (LPBF) from elementally blended powders. *Materials* **2022**, *15*(9), 3304.
16. Khairallah, S. A.; Anderson, A. T.; Rubenchik, A.; King, W. E. Laser powder-bed fusion additive manufacturing: Physics of complex melt flow and formation mechanisms of pores, spatter, and denudation zones. *Acta Materialia* **2016**, *108*, 36–45.
17. Ceccanti, F.; Giorgetti, A.; Arcidiacono, G.; Citti, P. Laser powder bed fusion: A review on the design constraints. In Proceedings of the *IOP Conference Series: Materials Science and Engineering*; IOP Publishing, 2021; Vol. 1038, No. 1, p. 012065.
18. Kempen, K.; Thijs, L.; Van Humbeeck, J.; Kruth, J.-P. Mechanical properties of AlSi10Mg produced by selective laser melting. *Phys Procedia* **2012**, *39*, 439–446.
19. Zhang, J.; Li, B. The Influence of Laser Powder Bed Fusion (L-PBF) Process Parameters on 3D-Printed Quality and Stress–Strain Behavior of High-Entropy Alloy (HEA) Rod-Lattices. *Metals (Basel)* **2022**, *12*(12), 2109, doi:10.3390/met12122109.
20. Palchik, V.; Hatzor, Y. H. The influence of porosity on tensile and compressive strength of porous chalks. *Rock Mechanics and Rock Engineering* **2004**, *37*, 331–341.
21. Rastan, H.; Abdi, A.; Hamawandi, B.; Ignatowicz, M.; Meyer, J. P.; Palm, B. Heat transfer study of enhanced additively manufactured minichannel heat exchangers. *International Journal of Heat and Mass Transfer* **2020**, *161*, 120271.
22. Gong, H.; Rafi, K.; Gu, H.; Starr, T.; Stucker, B. Analysis of defect generation in Ti–6Al–4V parts made using powder bed fusion additive manufacturing processes. *Additive Manufacturing* **2014**, *1*, 87–98.
23. Du Plessis, A.; Yadroitsava, I.; Yadroitsev, I. Effects of defects on mechanical properties in metal additive manufacturing: A review focusing on X-ray tomography insights. *Materials & Design* **2020**, *187*, 108385.
24. Rahman, M. E.; Weibel, J. A. Influence of convective heat transfer and wall thermal capacity on dynamic interactions between wall temperature and pressure drop oscillations during microchannel flow boiling. *International Journal of Heat and Mass Transfer* **2024**, *221*, 125111.
25. Kraus, H.; Bilodeau, G. G.; Langer, B. F. Stresses in thin-walled pressure vessels with ellipsoidal heads, 1961.
26. Silva, E. C.; Candiango, J. A.; Rodrigues, S. J.; Sampaio, Á. M.; Pontes, A. J. Hybrid Manufacturing of Aluminium Parts Combining Additive and Conventional Technologies—Mechanical and Thermal Properties. *Journal of Manufacturing and Materials Processing* **2022**, *6*(2), 40.
27. Lv, F.; Shen, L.; Liang, H.; Xie, D.; Wang, C.; Tian, Z. Mechanical properties of AlSi10Mg alloy fabricated by laser melting deposition and improvements via heat treatment. *Optik* **2019**, *179*, 8–18.
28. Jing, C.; Hou, W.; Wang, X.; Chu, S.; Yang, Z. Microstructure, porosity and mechanical properties of selective laser melted AlSi10Mg. *Chinese Journal of Aeronautics* **2020**, *33*(7), 2043–2054.
29. Lind, N. C. Consistent partial safety factors. *Journal of the Structural Division* **1971**, *97*(6), 1651–1669.
30. Chai, L.; Xia, G.; Zhou, M.; Li, J.; Qi, J. Optimum thermal design of interrupted microchannel heat sink with rectangular ribs in the transverse microchambers. *Applied Thermal Engineering* **2013**, *51*(1-2), 880–889.
31. Wang, Y.-Z.; Li, G.-Q.; Wang, Y.-B.; Lyu, Y.-F. Simplified method to identify full von Mises stress-strain curve of structural metals. *Journal of Constructional Steel Research* **2021**, *181*, 106624.
32. Amstutz, S.; Novotny, A. A. Topological optimization of structures subject to von Mises stress constraints. *Structural and Multidisciplinary Optimization* **2010**, *41*, 407–420.